Neutron-Detected Tomography of Impurity-Seeded Superfluid Helium

M. E. Hayden,[1] G. Archibald,[1] P. D. Barnes,[2] W. T. Buttler,[2] D. J. Clark,[2] M. D. Cooper,[2] M. Espy,[2] R. Golub,[3]
G. L. Greene,[4] S. K. Lamoreaux,[2] C. Lei,[1] L. J. Marek,[2] J.-C. Peng,[5] and S. I. Penttila[2]
[1]*Physics Department, Simon Fraser University, 8888 University Drive, Burnaby, British Columbia, Canada V5A 1S6*
[2]*Physics Division, Los Alamos National Laboratory, Los Alamos, New Mexico 87545, USA*
[3]*Hahn-Meitner Institut, Glienicker Strasse 100, D-14109 Berlin, Germany*
[4]*Department of Physics, University of Tennessee, Knoxville, Tennessee 37966, USA*
[5]*University of Illinois at Urbana Champaign, 1110 West Green Street, Urbana, Illinois 61801-3080, USA*
(Received 9 January 2004; published 3 September 2004)

We describe a neutron radiography technique that can be used to map the distribution of ^{3}He impurities in liquid ^{4}He, providing direct and quantitative access to underlying transport processes. Images reflecting finite normal- and superfluid-component ^{4}He velocity fields are presented.

DOI: 10.1103/PhysRevLett.93.105302 PACS numbers: 67.60.–g, 47.37.+q, 47.80.+v, 67.90.+z

The spectacular macroscopic quantum behavior exhibited by liquid helium (ℓ-^{4}He) at temperatures below 2.17 K has fascinated physicists since evidence for hydrodynamic flow without dissipation, the hallmark signature of a superfluid, was first announced in 1938 [1]. To this day superfluidity in liquid helium [2,3], and more generally in quantum fluids [4], constitutes an important discipline of research with broad implications, from understanding neutron stars [5] to developing atomic lasers [6]. Despite the maturity of the field, it has proven remarkably difficult to "map" or "image" superfluid flow in ℓ-^{4}He with significant spatial resolution. In part, this is because the liquid is naturally self-cleaning. At low temperatures, almost any neutral atom or molecule (other than ^{3}He) that is injected as a contrast agent will aggregate in the bulk or adsorb to the walls of the container. Here we report a neutron radiography technique that has enabled the first-ever multidimensional tomographic visualization of ^{3}He impurity distributions in superfluid ℓ-^{4}He (Helium II). At temperatures of order 1 K these impurities couple to the normal (nonsuperfluid) component of the liquid, allowing us to probe the underlying ^{4}He velocity fields with millimeter-scale resolution.

A variety of impurity-seeding techniques have previously been employed in the study of ℓ-^{4}He [7]. Charged impurities such as ions and electrons can be implanted into superfluid ℓ-^{4}He and subsequently imaged or tracked with exquisite resolution, but interact strongly with the host liquid, vortices, other charged impurities, and externally applied electromagnetic fields [8]. Clouds of bubbles formed during ultrasonic cavitation experiments produce a dramatic increase in optical scattering and can be directly photographed, but ultimately probe the acoustic radiation field and the thermodynamic properties of the liquid rather than underlying transport phenomena [9]. Particle image velocimetry techniques have even been used to study small (1–10 μm) neutrally buoyant tracer particles in ℓ-^{4}He, but to date these experiments have been restricted to temperatures above the superfluid transition [10]. Our work using ^{3}He as a neutral, minimally invasive, neutron-absorbing impurity is based on a proposal made in an appendix to Ref. [11], and makes use of an apparatus that has been described previously in the context of measurements of the mass-diffusion coefficient of ^{3}He in superfluid ℓ-^{4}He [12,13].

The experimental cell at the heart of our neutron-tomography apparatus is shown in Fig. 1. It is a 100 cm^3

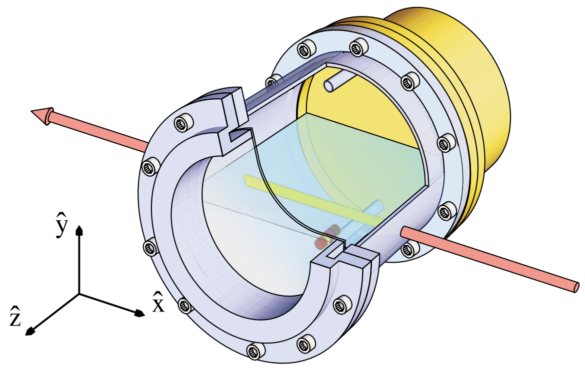

FIG. 1 (color online). Cutaway view illustrating the geometry of the experimental volume. A collimated neutron beam directed along the *x* axis passes through a 5 cm diameter Al cell, which is mounted to the mixing chamber of a moveable dilution refrigerator. The axis of the cell is nominally aligned with the *z* (horizontal) coordinate and can be moved in the *y*-*z* plane. Helium is admitted through a 1.5 mm diameter constantan fill tube that is thermally anchored to the mixing chamber of the refrigerator and penetrates the OFHC Cu end-wall 3 mm from the top of the cell. A resistive heat source is mounted near the midpoint of the base of the cell, while a calibrated resistance thermometer (not shown) is located on the axis of the cell near the mixing chamber wall. The origin of the coordinate system is chosen as the midpoint of the OFHC Cu wall abutting the mixing chamber. The opposite end-wall is a fused silica optical window that permits light originating from within the cell to be detected by a photomultiplier tube. The cell is shown here in a half-filled state.

right-cylindrical volume mounted to the mixing chamber of a dilution refrigerator and aligned such that its axis is both horizontal and orthogonal to a narrow and well-collimated neutron beam generated by a pulsed spallation source. The dilution refrigerator is in turn mounted to a translation table equipped with linear resistive displacement transducers. This arrangement provides for accurate and reproducible two-dimensional positioning of the cell in the plane orthogonal to the neutron beam.

The cell can be filled to an arbitrary depth with dilute solutions of ^{3}He in ℓ-^{4}He by condensing gas of the appropriate mixture through a narrow fill tube that penetrates the Cu wall abutting the mixing chamber of the refrigerator. As the beam passes through the cell, neutron-capture on ^{3}He nuclei results in the production of protons and tritons; these reaction products ultimately lead to the production of 80 nm (XUV) scintillation light as they are brought to rest in the liquid over distances of order 100 μm. A tetraphenyl butadiene coating deposited on the walls of the cell down-converts the XUV scintillation light into the visible range (450 nm) where it is readily detected using a photomultiplier tube [14]. The latter is mounted to the wall of the cell opposite the mixing chamber, and separated from the ℓ-^{4}He by a series of optical windows and vacuum spaces designed to minimize the heat load on the refrigerator. The photomultiplier tube count rate is thus expected to reflect the volume-integrated density of ^{3}He atoms encountered by the neutron beam as it passes through the cell. Typically we operate with fractional ^{3}He concentrations X of order 10–100 ppm, which is sufficient to absorb up to 10% of the incident neutrons. Note that the spatial resolution of our experiments is at present limited by the size of the neutron beam, as illustrated in Fig. 2.

During our experiments we also monitor the proton current delivered to the tungsten spallation target and the flux of neutrons transmitted through the cell. The latter is accomplished using a ^{6}Li-doped-glass scintillation neutron detector positioned immediately downstream of the experimental cell. The proton current serves as an overall normalization factor to account for fluctuations in the intensity of the neutron beam incident on the cell, while the ^{6}Li-glass detector allows us to quantify effects associated with extraneous scattering and absorption of the beam. For the work reported here all detectors were gated to discriminate scintillation and transmission events by the time-of-flight required for cold (2.5–3.6 Å) neutrons to arrive from the spallation source. Typical gated counting rates for the ^{6}Li-glass counter were of order 1 kHz.

We determine the absolute position and alignment of the cell with respect to the neutron beam and with respect to the axes of the translation system by observing the neutron-induced scintillation rate and the neutron transmission rate as a function of position near the periphery of the cell. Sharp features associated with the upper and lower extent of the cell, the mixing chamber wall, and the fused silica optical window combined with the known geometry of the cell and the intensity distribution of the neutron beam provide an absolute measurement of the relative positioning of the cell and beam. These data are further enhanced when the cell is only partially filled, providing a free liquid surface that clearly demarcates the alignment of the entire apparatus with respect to the horizontal. Ultimately this information allows us to accurately determine the geometric length of the neutron beam trajectory through the cell. Examples of such data are presented in Ref. [13].

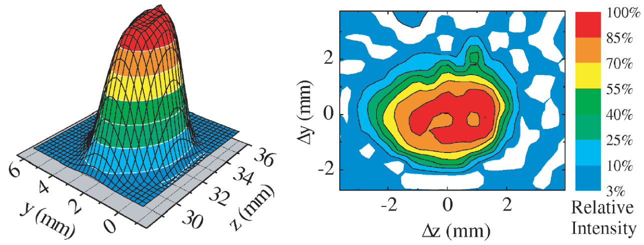

FIG. 2 (color online). Relative neutron beam intensity as a function of the transverse spatial coordinates. The data in the left half of this figure correspond to a measurement of the neutron transmission rate in the vicinity of a 1 mm diameter hole in a 0.5 mm thick sheet of (neutron-absorbing) Cd metal that was temporarily affixed to the upstream side of the experimental cell. The alignment of the hole was such that the collimated beam passed close to the center of the (full) cell before striking a ^{6}Li-doped-glass scintillation detector. The intensity profile of the incident beam that is inferred from these data (contour plot in right-half of figure) is slightly asymmetric, but well fit by Gaussian distributions with spatially averaged FWHM's of 2.5 and 3.5 mm in the vertical ($\hat{y}$) and horizontal ($\hat{z}$) directions, respectively. The divergence of the neutron beam as determined in a separate measurement is less than 10^{-3} rad.

In our treatment of the data presented here we account for a number of systematic effects that would otherwise influence an absolute determination of the average ^{3}He concentration in the cell at the level of 10–20%. For example, we observed a position-dependent (but neutron independent) background scintillation rate associated with the intense gamma and energetic charged particle pulse generated by the spallation source. We also observed absorption and/or scattering of neutrons by the Al walls and flanges of the cell, the Al radiation shields and vacuum cans associated with the refrigerator, other structural elements of the cell (OFHC Cu end-wall, fused silica window, constantan fill tube and heater support), and the ℓ-^{4}He itself [15]. Both of the latter effects influence the neutron transmission rate, while decay products resulting from neutron absorption also produce an activation-induced position- and time-dependent background scintillation rate.

After subtracting position-dependent background signals and using the ^{6}Li-glass detector to correct for absorption and scattering we are able to measure the residual detection efficiency η of our apparatus for neutron-induced scintillation events in the ℓ-^{4}He. This measurement is performed after cooling the cell well below 1 K (typ. 400–600 mK) where the diffusivity of ^{3}He in ℓ-^{4}He is large [12,16], ensuring a highly uniform impurity-atom distribution. We find empirically that if the photomultiplier tube count rate is normalized by the geometric path length $\sqrt{1-(y/R)^2}$ of the beam through the cell, the detection efficiency is largely independent of the vertical coordinate y, temperature, and the ^{3}He concentration X, and that it varies as $\eta = \eta_0(1 - z^2/L^2)$ along the horizontal coordinate z. Here R is the radius of the cell and the length scale L is of order 6 cm. The detection efficiency near the optical window is thus about 40% that of the peak efficiency η_0 near the mixing chamber wall.

As the temperature is raised to 1 K the distribution of ^{3}He impurities remains uniform, and the gross features of the background- and sensitivity-corrected scintillation rate continue to reflect the geometric length of the neutron beam path through the cell. Under these conditions the ^{3}He mean free path is of order 1 μm [12]. In order to illustrate a more substantive application of this imaging technique, an electrical current was passed through the resistive heater located near the bottom of the cell. This has the effect of driving a heat current between the heater and the mixing chamber of the refrigerator. In terms of the two-fluid model for helium II, this heat current is carried by the normal component of the liquid [2]. The ^{3}He impurities in the cell act as tracer particles that are carried along with the convecting fluid [17]. Microscopically, they scatter from excitations associated with the heat flow. Their steady-state distribution (which results from the competing effects of forced convection and diffusion) satisfies $\nabla \ln X = \mathbf{v}_n/D$ [12], where $\mathbf{v}_n$ is the velocity of the normal component of the liquid and D is the impurity-atom mass-diffusion coefficient. Alternately, $\nabla \ln X = \mathbf{q}/\rho s T D$ where ρ, s, and T are the ^{4}He density, entropy, and temperature, and $\mathbf{q}$ is the heat flux transported by the liquid. In other words, measurements of the spatial variation of the ^{3}He concentration X probe the heat flux or equivalently, the velocity of the normal component of the fluid. Mass conservation implies that these data can also be thought of as a probe of the superfluid-component of the liquid. These concepts are illustrated in Fig. 3, which shows the results of a model calculation for a simplified geometry, and two images generated from gray scale mappings of tomographically determined ^{3}He impurity distributions in our experimental cell. Figures 3(a) and 3(b) clearly indicate that a substantial reduction in the concentration of ^{3}He occurs in the immediate vicinity of the heat source.

Figure 3(c) shows data that provides remarkable insight into a phenomenon known as the HEVAC effect [18]. Under partial filling conditions at temperatures of 1 K and higher, the application of a heat current drives most

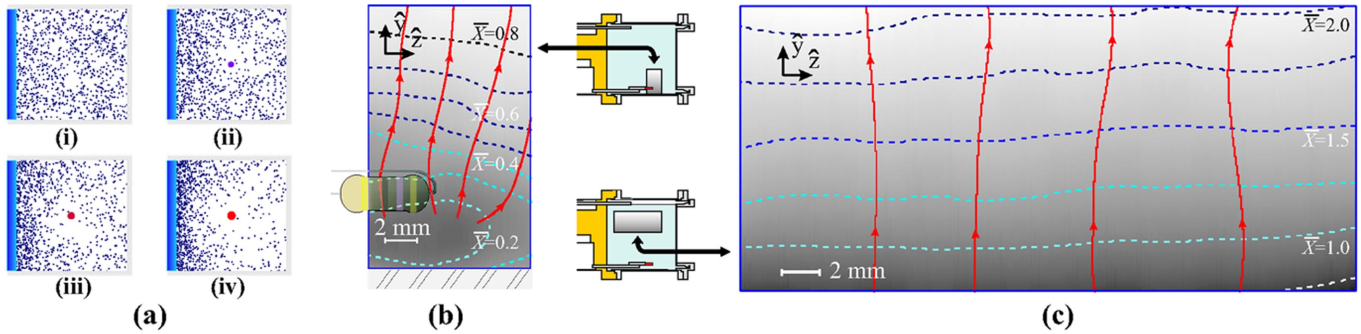

FIG. 3 (color online). Neutron-tomography images. Under our experimental conditions (very low heat flux, very low ^{3}He concentration, laminar flow) the normal component of the liquid undergoes potential flow; that is $\mathbf{v}_n = \nabla\Phi$ where the velocity potential Φ satisfies Laplace's equation $\nabla^2\Phi = 0$. This leads to a ^{3}He distribution $X = C\exp(\Phi/D)$, where C is a geometry-dependent normalization factor [12]. Figure 3(a) shows a simple two-dimensional model calculation illustrating the effect that a heat current $\dot{Q}$ has on the distribution of ^{3}He atoms (dots) confined to a square cell with a single wall (left side) that acts as a perfect heat sink. The competing effects of forced convection and diffusion lead to the formation of a progressively larger ^{3}He-depleted zone in the vicinity of the centrally-located heater as $\dot{Q}$ is increased [subpanels (i) through (iv)]. Figure 3(b) shows data representing the relative ^{3}He concentration integrated along the path of the neutron beam ($\bar{X}$) in the lower-half of our experimental cell near the heater at 0.92 K. A gray scale mapping of the ratio of the background-subtracted neutron-induced scintillation rates measured with and without $\dot{Q} = 5$ mW was used to generate this image. Dark regions correspond to low ^{3}He concentrations. Dashed and labeled contour lines (representing $\bar{X}$) and solid streamlines (representing the average direction of $\mathbf{q}$ or $\mathbf{v}_n$) have been drawn to illustrate the manner in which these experiments probe the underlying (three-dimensional) velocity fields. Figure 3(c) shows data representing $\bar{X}$ in the upper-half of the cell at 0.99 K when a free liquid surface is introduced and $\dot{Q} = 14$ mW; the imaged region extends to within 5 mm of the surface, which was in turn located immediately below the fill tube. A dramatic and uniform gradient in the ^{3}He concentration directed toward the liquid surface is evident. These data reflect a relative concentration resolution of order 2%, and imply normal and superfluid velocities of order 10^{-1} and 10^{-3} cm/s, respectively. Scale drawings of the experimental cell [inserted between Figs. 3(b) and 3(c)] indicate the location and extent of the imaged regions.

of the ^{3}He impurities in the cell to the free liquid surface rather than to the Cu wall abutting the mixing chamber of the refrigerator. This is direct experimental evidence that the thermal conductances of the narrow vapor-filled tube passing through the Cu wall and the vapor-filled channel above the liquid are large compared to the thermal conductances presented by the Cu wall and the bulk superfluid ℓ-^{4}He in the cell, respectively. In effect the two vapor-filled channels act as low-temperature heat pipes, with heat transfer being accomplished by the evaporation and subsequent condensation (at a distance) of ^{4}He atoms and limited only by the (laminar) hydrodynamic flow impedance of the channel [18]. These data also provide direct experimental evidence for a normal component velocity (and by inference a superfluid-component velocity) directed perpendicular to a free liquid surface, and highlight the ease with which highly nonuniform and alarmingly nonintuitive impurity-atom distributions can be generated in such situations.

This work demonstrates the essential features of a new experimental technique that allows one to generate high-resolution images of impurity distributions and velocity fields in superfluid liquid ^{4}He seeded with minute quantities of ^{3}He. Unlike previous imaging techniques, our methods provide direct access to underlying transport phenomena in this archetypal quantum system. We anticipate that significant improvements can be made to the quality of data derived from such experiments with attention to systematic uncertainties associated with the extraneous absorption and scattering of neutrons (materials selection, cell geometry, and longer wavelength neutrons). Larger neutron fluxes, smaller beam diameters, and the use of polarized neutrons and impurities should also yield improvements, and may facilitate both time-resolved and spin-resolved measurements of impurity distributions.

The methods introduced here suggest a wealth of opportunity for refinement and future study of fundamental problems in condensed matter physics. For example, at present ^{3}He and ^{2}H are the only two neutral atom impurities in superfluid liquid ^{4}He for which effective mass data exists [2,19]. Measurements of the diffusivity of other neutral (neutron-absorbing) impurities in liquid ^{4}He such as ^{6}Li could yield a very substantial advance in our understanding of local superfluid dynamics and impurity-background correlations in inhomogeneous quantum systems [20]. Likewise, NMR imaging techniques used in conjunction with neutron-detected tomography would permit precision comparisons of spin- and mass-diffusion phenomena [21]. It is evident that neutron-detected tomography provides an excellent probe for monitoring impurity distributions, for studying heat transfer, and for mapping hydrodynamic velocity fields. In principle similar experiments should enable one to explore situations in which quantized vortex filaments are introduced, critical superfluid velocities are intentionally exceeded, ultrahigh values of Reynolds and Raleigh numbers are achieved, and the adsorption of impurities to surfaces is considered. Examples of topical problems to which these techniques might be applied include investigations of Rayleigh-Bénard convection [22] and quantum turbulence [23].

We are indebted to P. V. E. McClintock for suggesting the use of XUV scintillation light to study the interaction of neutrons with ^{3}He impurities. This work was performed using flightpath 11A at the Los Alamos Neutron Science Center, and was funded by Los Alamos National Laboratory (LDRD-DR2001526) and NSERC (Canada).

[1] J. F. Allen and A. D. Misener, Nature (London) **141**, 75 (1938); P. Kapitza, Nature (London) **141**, 74 (1938); also see S. Balibar, Bull. Soc. Fr. Phys. **128**, 14 (2001).
[2] E.g., J. Wilks and D. S. Betts, *An Introduction to Liquid Helium* (Clarendon Press, Oxford, 1987).
[3] J. P. Toennies, A. F. Vilesov, and K. B. Whaley, Phys. Today **54**, No. 2, 31 (2001).
[4] E.g., P. Nozières and D. Pines, *Superfluid Bose Liquids*, The Theory of Quantum Liquids Vol. II (Perseus Books, Cambridge MA, 1999); A. Griffen, D.W. Snoke, and S. Stringari, *Bose-Einstein Condensation* (Cambridge University Press, New York, 1995).
[5] E.g., D. J. Dean and M. Hjorth-Jensen, Rev. Mod. Phys. **75**, 607 (2003).
[6] E.g., M. R. Andrews *et al.*, Science **275**, 637 (1997).
[7] B. Tabbert, H. Günther, and G. zu Putlitz, J. Low Temp. Phys. **109**, 653 (1997).
[8] G. A. Williams and R. E. Packard, Phys. Rev. Lett. **33**, 280 (1974); M. S. Khaikin, J. Phys. (Paris), Colloq. **C-6**, 1295 (1978); B. Tabbert *et al.*, Z. Phys. B **98**, 399 (1995).
[9] M. S. Pettersen, C. Naud, S. Balibar, and H. J. Maris, Physica B (Amsterdam) **194B–196B**, 575 (1994).
[10] R. J. Donnelly *et al.*, J. Low Temp. Phys. **126**, 327 (2002).
[11] R. Golub and S. K. Lamoreaux, Phys. Rep. **237**, 1 (1994).
[12] S. K. Lamoreaux *et al.*, Europhys. Lett. **58**, 718 (2002).
[13] M. E. Hayden *et al.*, Physica (Amsterdam) **329B–333B**, 236 (2003).
[14] D. N. McKinsey *et al.*, Phys. Rev. A **67**, 62716 (2003).
[15] H. S. Sommers, Jr., J. G. Dash, and L. Goldstein, Phys. Rev. **97**, 855 (1955).
[16] R. M. Bowley, Europhys. Lett. **58**, 725 (2002).
[17] F. London, *Superfluids* (Wiley, New York, 1954), Vol. II.
[18] P. J. Nacher, M. Cornut, and M. E. Hayden, J. Low Temp. Phys. **97**, 417 (1994); M. E. Hayden, M. Cornut, and P. J. Nacher, Physica (Amsterdam) **195B–196B**, 677 (1994).
[19] M. E. Hayden and W. N. Hardy, J. Low Temp. Phys. **99**, 787 (1995).
[20] B. E. Clements, E. Krotscheck, and M. Saarela, J. Low Temp. Phys. **100**, 175 (1995).
[21] I. N. Adamenko and K. E. Nemchenko, Low Temp. Phys. **21**, 386 (1995).
[22] A. L. Woodcraft, P. G. J. Lucas, R. G. Matley, and W. Y. T. Wong, J. Low Temp. Phys. **114**, 109 (1999).
[23] W. F. Vinen and J. J. Niemela, J. Low Temp. Phys. **128**, 167 (2002).